Interferometer Scanning Microwave Microscopy: Performance Evaluation

Silviu-Sorin Tuca, Manuel Kasper, Ferry Kienberger, and Georg Gramse

***Abstract*—A systematic and quantitative comparison of electrical detection systems in scanning microwave microscopy is reported. Scanning microwave microscopy (SMM) is capable of investigating nanoscale electrical properties with high accuracy over a broad frequency range of 1–20 GHz. However, due to the passive matching network only discrete frequencies can be used every 1 GHz with varying signal-to-noise ratio (SNR). Here we study in detail the impedance matching mechanism using an interferometric network where a two-port measurement is implemented with a reduction of the trace noise due to signal subtraction. The interferometer setup shows superior performance resulting in a 2–8 fold increased SNR with respect to the standard shunt solution, in addition to stable broadband performance over the full frequency range. We perform a comparison of the electrical sensitivity obtained using a direct connection from the network analyser to probe, the typically implemented shunt-resonator impedance matching network, and the proposed interferometer setup. The interferometer SMM allows us also for calibrated impedance measurements, which we demonstrate on Tobacco mosaic viruses with 18-nm diameter, with a capacitance resolution of 0.67 attoFarads at 10 ms acquisition time per pixel.**

***Index Terms*—Hybrid coupler, interferometer, low noise amplifier (LNA), SMM.**

I. Introduction

SCANNING Microwave Microscopy (SMM) is a valuable tool that allows for simultaneous investigation of mechanical and high frequency electrical properties of materials at the nanoscale. To this end, it interfaces an atomic force microscope (AFM) with a vector network analyser (VNA). On the electrical measurement side, several sensing techniques have been proposed in literature [1]–[4]. In order to detect the extremely small electrical quantities exhibited by materials at the nanoscale, the high penetration rate of microwave radiation is used. Since typical dimensions of samples under test (SUT) are in μm to nm range, which are several orders of magnitude below the wavelengths of microwave radiation ($\sim$cm), SMM probes the perturbations of the quasi-static near-field in the SUT. This makes it possible to break the resolution limit of the wavelength of the probing microwaves and to resolve sample features with a lateral resolution down to nm range [2], theoretically limited only by the tip size.

However, in practice, SMM resolution and sensitivity are limited by the electrical detection system. There are several ways to excite and detect the electrical changes in the system. The near-field regime can be achieved using aperture-based or apertureless probes, including but not restricted to resonant cavities, open-ended waveguides, or half-wavelength resonators [2], [5], [6]. The changes in the formed evanescent waves can be detected at a single frequency, multi-frequency, or broadband. The variations of the resonator's Q-factor, the phase shift in frequency domain or the variation of the scattering S-parameters, all indicate a change in the electric properties under the probe, which are then calibrated to extract physical quantities [7]–[9].

Currently, the most versatile SMM studies in terms of frequency range can be performed using a VNA as excitation and detection tool. The high accuracy and high dynamic range of the VNA are used to measure S-parameters, which correlate to the sample's impedance as:

$$S_{11} = (Z_{SUT} - Z_{ref}) / (Z_{SUT} + Z_{ref}) \qquad (1)$$

with Z_{SUT} the sample impedance, and Z_{ref} the intrinsic 50 Ω VNA impedance, designed for 50 Ω network analyses. Consequently, it yields the best results when SUTs exhibit impedances close to 50 Ω. However, impedance values at the nanoscale are in the range of MΩ [10], thus negatively affecting the sensitivity of the measurements. An impedance matching network consisting of a 50 Ω shunt resistance and a half-wavelength resonator is used to create a standing wave pattern, whereby the impedance of the probe-sample system matches the 50 Ω of the VNA.

Nonetheless, the available frequencies where the impedance matching is achieved are limited by the design of the resonator. Additionally, the 50 Ω shunt limits the power transmitted to (and eventually reflected from) the SUT, thus limiting the achieved sensitivity to 1 aF at 100 Hz intermediate frequency bandwidth (IFBW). Thin-film semiconductors, single layer graphene, viruses of sub-micrometre sizes, and single molecules are some of the samples that have relative capacitances $<$1 aF, hence a detection scheme able to resolve capacitance values with higher accuracy is needed. Furthermore, the need of analysing biological samples in vitro or in vivo has pushed the implementation of a detection scheme with a

Manuscript received February 28, 2017; revised May 30, 2017; accepted June 28, 2017. Date of publication August 9, 2017; date of current version November 8, 2017. This work was supported in part by EU-FP7 (PEOPLE-2012-ITN-317116, NANOMICROWAVE), in part by the Bio-SMM FFG under Project 846532, and in part by FWF Project P 28018-B27. The review of this paper was arranged by associate editor Haixia (Alice) Zhang. *(Correspondence Author: Georg Gramse.)*

S.-S. Tuca and G. Gramse are with the Biophysics Institute, Johannes Kepler University, Linz 4040, Austria (e-mail: Silviu_Sorin.Tuca@jku.at; georg.gramse@jku.at).

M. Kasper and F. Kienberger are with the Keysight Technologies Austria GmbH, Keysight Labs, Linz 4020, Austria (e-mail: manuel.kasper@keysight.com; ferry_kienberger@keysight.com).

Color versions of one or more of the figures in this paper are available online at http://ieeexplore.ieee.org.

Digital Object Identifier 10.1109/TNANO.2017.2725383

dynamic range and accuracy suitable for the dielectric relaxation of liquids [11], [12]. The interferometer-based sensing technique aims to solve these shortcomings by actively subtracting the reference impedance and thus can yield excellent matching for any desired frequency and sample, as has been first shown by Tanbakuchi *et al*. in [13], where the similarity with a Mach-Zehnder interferometer is pointed out. We performed a systematic and quantitative comparison of signal-to-noise ratios (SNR) obtained with the standard 50 Ω shunt solution and different interferometer hardware approaches. We discuss the various noise sources and compare the theoretically-estimated with experimental measurements. This study can be seen as a noise performance benchmark of different detection schemes, using the same microscope, probe tip, and sample. Finally, the best hardware configuration, employed at the optimal power level, was used for an imaging application that had previously pushed the limits of standard SMM sensitivity.

II. Theory: Noise Contributions

The idea of implementing an interferometer-based signal detection scheme stemmed from studies made by several research groups working on various RF applications related [14]–[18] or unrelated to SMM [19], [20]. It is featured in [21] in a setup for ultrahigh sensitivity Ferromagnetic Resonance Measurement (FMR), where the authors explain in terms of noise and sensitivity benefits the reasoning behind adopting the Mach-Zehnder interferometer.

They identify three main noise sources in FMR measurements:

1) Trace noise
2) VNA receiver noise
3) Intermodulation distortion (IMD) induced by the VNA stimulus generator.

Trace noise represents the uncertainty associated with the receiver readouts, and it is minimised by minimising the IFBW and thus the scan speed. However, being a fixed specification of the VNA it has a minimum, which, in some applications, limits the sensitivity of the measurements. By subtracting the reference signal from the SMM readout signal, the Mach-Zehnder interferometer SMM (mziSMM) approach provides a trace noise free signal input to the receiving port of the VNA.

From the well-known RF and propagation theory Friis formula shown below, it can be inferred that the first stage in an RF signal detection scheme has the largest contribution on noise levels introduced in the system. Hence, by adding a low noise amplifier (LNA) as the first stage of the receiver, the benefit is two-fold: reducing the noise at this step, and downscaling the overall noise factor of the following stages in the detector *G*-fold, where G is the gain of the LNA, and F_{LNA} and F_{rec} are noise factors of LNA and the VNA receiver, respectively:

$$\boldsymbol{F_{tot} = F_{LNA} + (F_{rec} - 1)/G} \tag{2}$$

Once these two noise sources are mitigated, a downgrading of the SNR has been noticed in correlation with increasing input power values. This is due to the IMD present at 2nd and 3rd harmonics, due to the local oscillator of the VNA.

Similar RF arrangement has been used in [19], [20] emphasizing the benefits of this setup in impedance measurements. The sensitivity of this method is proved in [22] by analysing phase-resolved spin-resonance spectroscopy on magnetic materials. [16], [17] demonstrate the implementation of interferometer with SMM, for extreme impedance measurements.

III. Experimental Setup

The commercially available Keysight SMM uses a 50 Ω shunt along with a half-wavelength (λ/2) resonator to match the impedance of the SUT to the impedance of the VNA. Impedance calibration has been achieved by means of a calibration workflow [9]. The models proposed in [9], [23]–[26] for extraction of relative capacitance and conductance are applied on high-κ dielectrics, semiconductors and biological materials, with an obtained capacitance and conductance resolution of 1 aF, and 1 microSiemens (μS), respectively. The VNA has been used for the generation and detection of the high frequency electrical signal. In the direct connection setup, the SMM probe is connected to port 1 of the VNA via transmission line and adapters, as shown in Fig. 1(a). In this setup, the VNA measures the S_{11} signal. A frequency sweep over the full range of the VNA, 1–20 GHz, can be observed in Fig. 2(a), plotted in black. Since no impedance matching network is used and the ensemble made of SMM probe and nosecone has impedance much higher than 50 Ω, the poor impedance matching leads to a lack of standing waves, and therefore of notches in the frequency domain, along with a ripple pattern and a tendency of increasing attenuation with increasing frequency, due to the long transmission line used.

The performance of the electrical sensing technique can be thus improved to harvest the full potential of the VNA accuracy. To this end, an impedance matching network has been designed, including a broadband 50 Ω shunt, and a half-wavelength (λ/2) resonator, as seen in Fig. 1(b). This network matches the impedance downstream from it, i.e., the nosecone holding the SMM probe, in contact with the SUT, to 50 Ω, hence generating in the frequency domain a pattern of deep notches every 1 GHz (Fig. 2(a), plotted in red), whereby the SMM measurements are performed with best accuracy.

The physical length of the λ/2 resonator is 9 cm by design. This is directly related to the 900 MHz frequency span between the notches, by the relation $\lambda = v_p/f$ with v_p the speed of propagation in the transmission line, and f the frequency. For the investigated implementation v_p is roughly $C_0/2$ with C_0 being the speed of light.

This approach yields the optimal impedance matching and thus good SNR for SMM measurements deep down the notches. However, outside those created notches, the performance degrades rapidly. Additionally, the fixed design of the resonator is a limitation for broadband measurements.

In order to circumvent some of these limitations, an alternative sensing technique proposed in [14] and implemented in [16] allows for active notch seeking. It employs both VNA ports, one for signal generation, the other for SMM signal detection. The advantage of using two ports lies in the correction of directivity

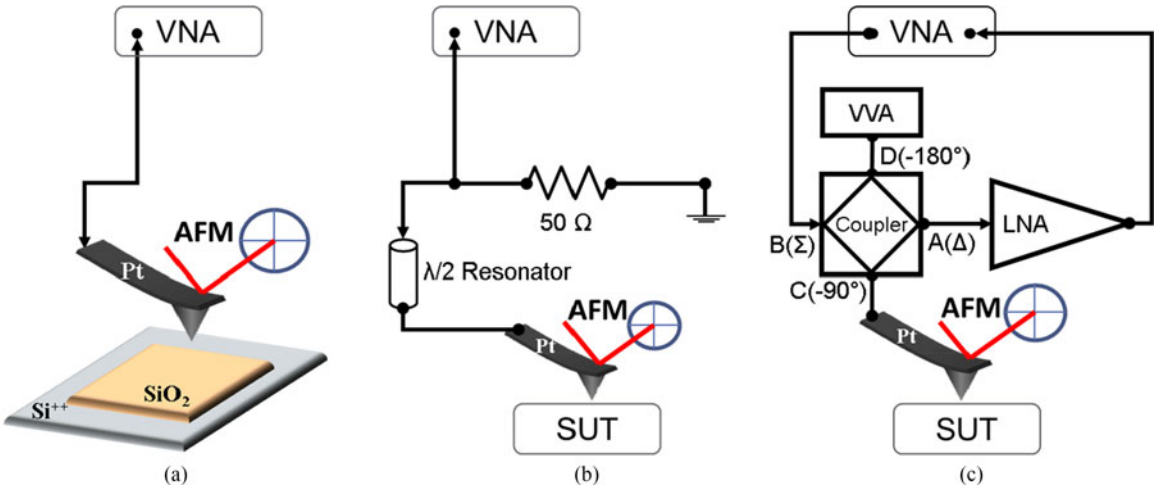

Fig. 1. SMM setup overview. (a) Schematic diagram showing the setup of AFM interfaced with VNA using direct connection by means of a coaxial cable from VNA port 1 to the nosecone holding the conductive AFM/SMM probe. (b) Diagram of standard Keysight SMM setup featuring λ/2 resonator and 50 Ω shunt as impedance matching network, between VNA and conductive SMM probe. (c) Diagram of interferometer detection scheme, involving 2-port VNA measurements, with signal output from VNA port 1, travelling to hybrid coupler, whereby it splits between ports C and D. The signal travelling the path via port C collects information about the sample, whereas the signal via port D is attenuated by VVA in a similar fashion to the nosecone path. The 2 reflected signals travel back to the hybrid coupler via ports C and D, and their sum is found at port B, whereas their difference at port A. Provided that the VVA tuning performed with the tip out-of-contact replicates the nosecone path best, the differences of the 2 reflected signals, output from port A, will stem only from the tip-sample interaction. This difference signal is then amplified using a broadband LNA, and sent to VNA port 2, where S_{21} is measured.

error, which is much smaller than in one-port measurements [27]. The sensing technique includes, in its most compact implementation, a 90-deg hybrid coupler (similar implementations with 180-deg hybrid couplers or 2 separate directional couplers [16] are also possible). As seen in Fig. 1(c), the signal output from VNA port 1 travels to sum (Σ) port of the hybrid coupler. Here, the signal splits between ports C and D. One of the branches is connected to nosecone and the SMM probe in contact with the SUT. The other branch is input to a voltage variable attenuator (VVA), used to replicate a transmission line with the same properties as the nosecone path. The signals reflected from both branches, input in their respective ports, are summed at the (Σ) port and subtracted at the difference (Δ) port. The signal at (Δ) port is then input to the broadband LNA with 30 dB gain, which amplifies the difference signal. The amplified output signal travels via transmission line to VNA port 2, where S_{21} is measured.

With the probe out of contact of the SUT, the VVA is tuned such that the frequency response replicates the nosecone's response for the desired measurement frequency. As the 2 reflected signals interfere destructively at (Δ) port, their difference is nought at frequencies where impedances match. When the SMM probe is in contact with the SUT, the SUT impedance will influence the signal reflected on the nosecone branch. As the signal reflected on the VVA branch matches the signal reflected from the nosecone alone, the resulting difference signal will only contain the effect of SUT impedance. Since the impedance differences at the SUT level are minute, the difference signal is close to the noise floor of the VNA, so it requires reconditioning by amplification, provided by the external LNA. As seen in the frequency sweep in Fig. 2(c), plotted in blue, the LNA shifts the S_{21} response above 0 dB, but the impedance-matching notches are relatively deeper than the ones obtained with standard shunt technique, hence theoretically providing better SNR for SMM measurements. The second major advantage is that notches can be tuned more freely by VVA manipulation, thus enabling quasi-broadband measurements.

IV. Interferometer-SMM: Imaging Test Samples

To precisely quantify the performance of the interferometer-based sensing technique we tested a set of samples. The control sample is made of Si^{++} substrate, onto which a SiO_2 staircase pattern is deposited. The pattern has well-defined height, increasing from 50 nm to 200 nm in steps of 50 nm each, and length and width of 50 μm.

In Fig. 3, the shunt and interferometer setups compare in terms of imaging SNR. Images of the same Si/SiO_2 staircase sample were acquired using the same SMM probe, using both setups. The typical AFM topography image is unaltered, but the performance of the detected electrical signal differs between the two sensing solutions. Both scans have been performed at a randomly chosen frequency notch, 6.3 GHz. The S_{11} or S_{21} amplitude and phase images presented have been flattened for both techniques. The cross-section of the images has been conditioned by assembling the complex S_{11} or S_{21} signal, calculating its magnitude, and normalising it. The normalised magnitude profile shown in Fig. 3(d) proves that imaging follows the results predicted from theory that the interferometer setup yields better SNR compared to standard shunt setup.

V. Quantitative Comparison of SNR Performance

Since the imaging mode of SMM validates the overall assumption that the SNR obtained using interferometer approach is better than using the shunt, we systematically confirmed for SMM the theoretical predictions presented in [21], by investigating the effect of different interferometer hardware configura-

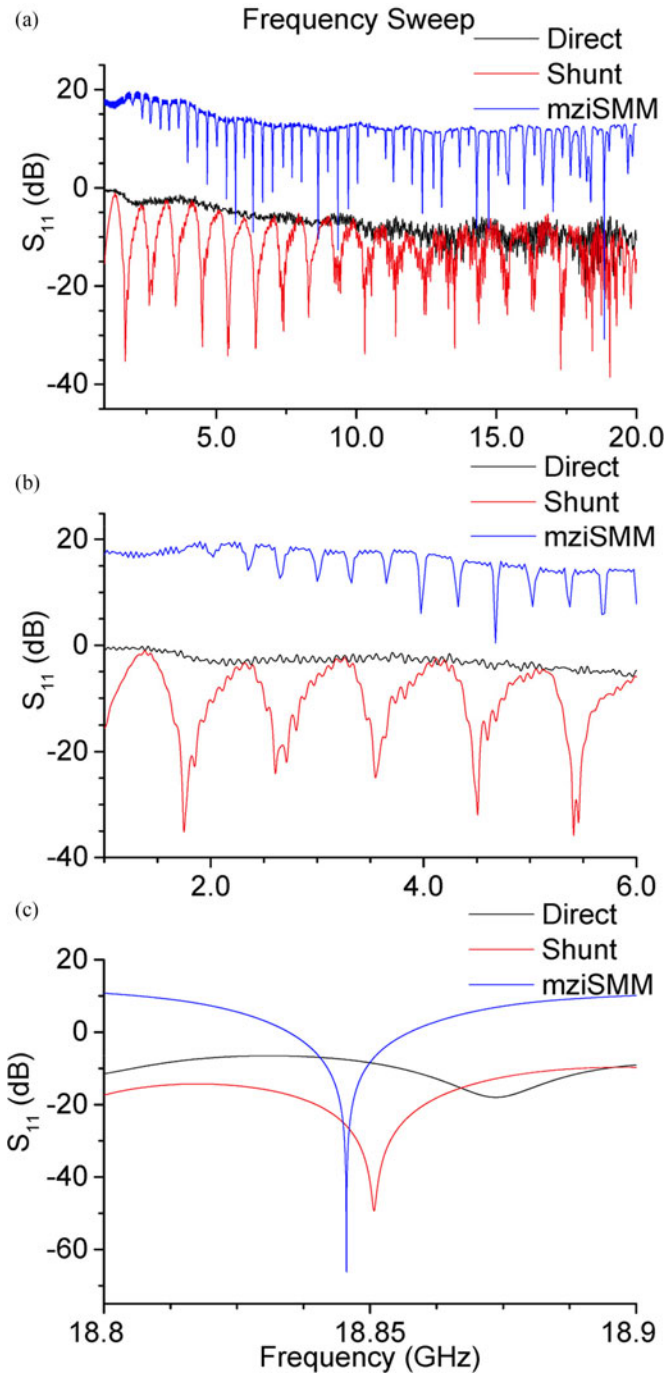

Fig. 2. Frequency sweep comparison. (a) Shows a comparison of the S_{11} (S_{21} in the interferometer case) vs. frequency for the setups in Fig. 1, recorded over the frequency range 1–20 GHz, with 500 Hz IFBW. (b) Comparison of the S_{11} and S_{21} values over the range 1–6 GHz, using similar settings. (c) Zoom-in of a deep notch at 18.9 GHz, emphasising the behaviour of the tuneable interferometer, which generates deeper notches compared to the other 2 techniques.

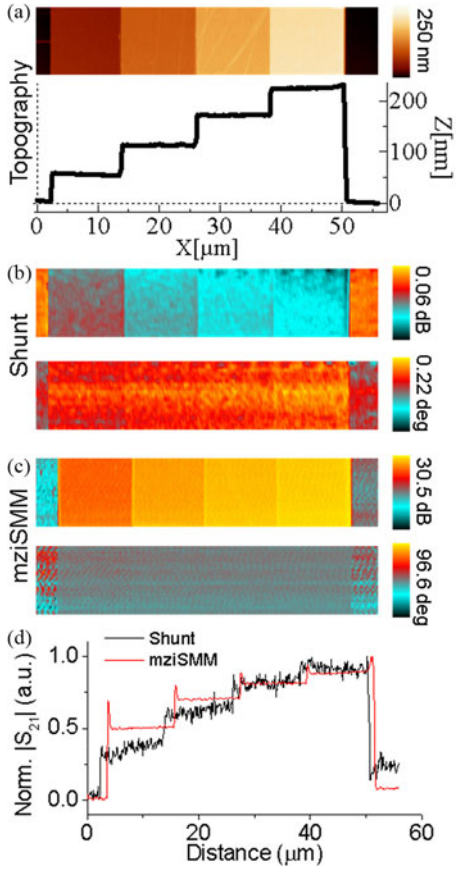

Fig. 3. Si/SiO_2 sample imaging comparison between the shunt technique and the proposed interferometer solution. (a) Upper panel: typical AFM topography image of SiO_2 staircase structure with heights from 50 nm to 200 nm deposited on Si substrate. Scale bar has 1 μm. Lower panel: cross-section over topography image of SiO_2 structured sample. (b) Upper panel: S_{11} amplitude signal obtained over the staircase structure using 50 Ω shunt setup. Lower panel: S_{11} phase signal obtained over the staircase structure with 50 Ω setup. (c) Upper panel: S_{21} amplitude signal of the staircase structure acquired with interferometer setup. Lower panel: S_{21} phase signal of staircase structure with interferometer setup. (d) Plotted comparison of the normalized magnitude of S_{11} and S_{21} profiles extracted from the 2 sensing techniques. It can be noticed that SNR of the profile taken from the interferometer scan is better compared to the SNR of the shunt technique.

tions on the observed SNR in a quantitative way. Therefore, the interferometer has been tested in several versions, changing the components included in the setup. Fig. 4 shows a comparison of the signal acquired in spectroscopy mode over bare Si^{++} on Si/SiO_2 pattern sample, using the standard 50 Ω shunt technique and 3 different versions of the interferometer technique, at a randomly chosen frequency, i.e., 5 GHz. The signal was acquired point-wise, by varying the tip-sample distance while recording the variation of S_{11} or S_{21} amplitude and phase signals. The spectroscopy curves were subjected to a conditioning similar to data presented in Fig. 3. In panel (a), the magnitude of normalized S_{11} (or S_{21}), is plotted against the tip-sample distance. In panel (b), the scatter plot in complex plane of the techniques is plotted. Again, the least spreading of the points suggests the best noise performance. Table I shows the corresponding SNR values calculated from spectroscopy curves presented in Fig. 4(a). In the 1st configuration, the 90-deg hybrid coupler is used as open-ended transmission line stub instead of VVA to balance the nosecone impedance. The stub length was chosen to be 9 cm, identical to the length of transmission line connecting the hybrid coupler to nosecone. As can be seen from Fig. 4 and Table I, the combination of hybrid coupler with the LNA (*mziSMM + LNA*) shows, with a calculated SNR of only 20, the

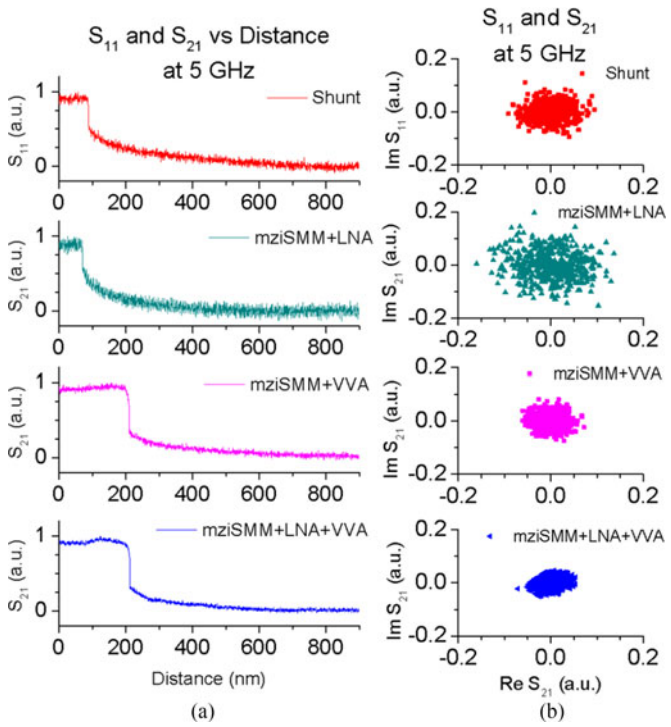

Fig. 4. Single-frequency SNR performance comparison. (a) Comparison of normalized and corrected S_{11} (or S_{21}) vs. distance curves, performed on bare Si. The approach curves have been performed using 4 different sensing techniques for the electrical measurements, as follows: the standard 50 Ω shunt SMM model and 1) hybrid coupler, with VVA on the balancing branch; 2) hybrid coupler with broadband LNA, and 3) hybrid coupler with VVA on the balancing branch and broadband LNA on the difference output. It can be observed that the setup with hybrid coupler, VVA, and LNA yields the best SNR results. (b) Scatter plot in the complex plane of S_{11} (or S_{21}) data shown in (a), which confirms the least spreading of data points acquired using the hybrid coupler-VVA-LNA scheme.

TABLE I
SNR AT A SINGLE FREQUENCY

Frequency (GHz)	Setup	SNR
5	Shunt	31
	mziSMM + LNA	20
	mziSMM + VVA	49
	mziSMM + VVA + LNA	63

Table I: SNR obtained from spectroscopy curves presented in Fig. 4. In agreement with the S_{11} or S_{21} magnitude vs. distance, and scatter plots, the interferometer setup including the VVA and the external LNA provides the best SNR of all the proposed interferometer-based setups, yielding twice the SNR obtained in the shunt measurement.

worst performance, since the interferometer is not well tuned and the LNA inputs additional noise to the receiver.

The 2nd setup represented the hybrid coupler used as signal divider and combiner, along with VVA on one of the branches; this setup lacks the LNA for the difference signal and is expected to yield a pattern of deep notches, but a very low signal at the VNA receiver. In the spectroscopy results from Fig. 4, the configuration *mziSMM + VVA* shows a considerably smoother curve and yields an SNR of 49, almost 2 times better, compared to the shunt ($\mathrm{SNR}_{\mathrm{shunt}} = 31$). The improvement is due to the improved tunability of the notch using the VVA, which enhances the impedance matching. However, in this configuration, the signal resulting from the destructive interference has power levels close to the noise floor of the VNA (−114 dB) [28].

TABLE II
SNR AT DIFFERENT POWER LEVELS

mziSMM + VVA + LNA		
Frequency (GHz)	Input power (dBm)	SNR
5	3	7
	0	21
	−3	59
	−6	63
	−9	57

Table II: SNR obtained from spectroscopy curves presented in Fig. 8. Higher power levels introduce a higher amount of noise in the system, whereas lower values of power provide an improvement of the SNR. The best performance observed using our setup is achieved at −6 dBm.

The 3rd tested version had the hybrid coupler as signal divider and combiner, with VVA balancing the nosecone impedance and external LNA, placed immediately at the output of the coupler. This configuration is meant for reducing noise sources 1 and 2 and should have the best performance. As expected, the resulted SNR with a value of 63 and 2x improvement over the shunt configuration is exhibited by the interferometer setup including the VVA and the external LNA. The LNA additionally lifts the signal 30 dB out of the VNA noise floor.

As stated in the Theory section, in contrast to the passive shunt implementation, in the interferometer setup we expect 2nd and 3rd order intermodulation products at high input power levels; these lead to additional noise when using active components like the LNA. In order to determine empirically the power threshold that allows for noise minimisation, we repeated the spectroscopy experiment that lead to the results presented in Fig. 4, using the best-observed detection setup, i.e., interferometer with LNA and VVA. The power level input from the VNA's transmission port varied from +3 dBm to −9 dBm. The results, shown in Fig. 8, in Appendix, have been analysed in the same way as the data shown in Fig. 4. The calculated SNR values obtained at the mentioned power levels are in Table II. We observed a maximum SNR at −6 dBm, with slightly weaker performance at −3 and −9 dBm. IMD introduces a high amount of noise in the system at higher input power, influencing the SNR, which drops to a figure of almost 10x less than the best result. IMD of 2nd and 3rd order comes from the local oscillator of the VNA in combination with the non-linearity of the LNA. Even though the interferometer cancels out the contribution at the measurement frequency, when the VNA stimulus is close to its saturation regime, i.e., at 3 dBm, the 2nd and 3rd order products cannot be filtered out. With the contribution of a non-linear LNA, the effect of these components is noticeable on the SNR of SMM measurements.

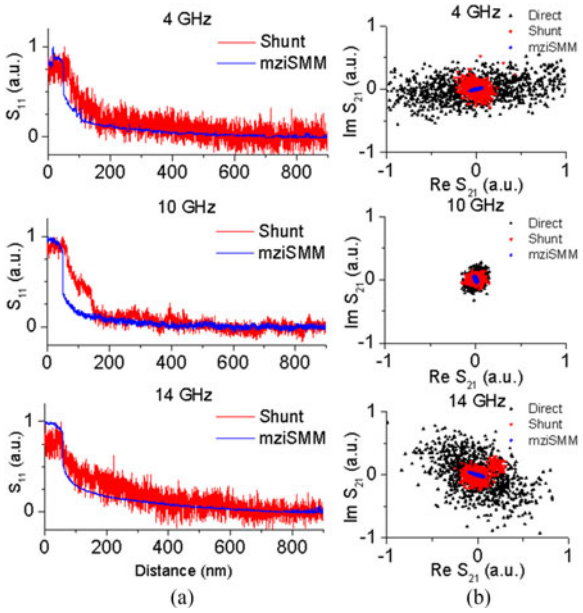

Fig. 5. Multi-frequency SNR performance comparison. (a) Normalised and corrected S_{11} (or S_{21}) vs. distance curves acquired using the 50 Ω shunt technique vs. interferometer detector, at 3 frequencies: 4 GHz, 10 GHz, and 14 GHz. (b) Scatter plots in complex plane of S_{11} (or S_{21}) of direct vs. shunt vs. interferometer schemes, at the same 3 frequencies.

TABLE III
MULTIFREQUENCY SNR

Frequency (GHz)	SNR Direct	SNR Shunt	SNR mziSMM
4	4.3	11.6	87.8
10	15.7	22.3	52.1
14	4.9	15.6	80.2

Table III: Calculated SNR values at 3 frequencies over SMM range: 4 GHz, 10 GHz, and 14 GHz, using direct connection, shunt, and interferometer setups. The values indicate that direct connection has the poorest SNR performance, while interferometer SNR is on average 2 times better than shunt SNR.

In order to test the broadband quality of SNR over the SMM frequency range, we performed a head-to-head comparison of the standard shunt setup vs. the best performing interferometer-based setup, at 3 different frequencies, i.e., 4 GHz, 10 GHz, and 14 GHz. The results are shown in Fig. 5. The left panel (a) shows the plotted S_{11} and S_{21} magnitudes, normalized as previously mentioned, vs. tip-sample distance. Panel (b) shows the complex plane scatter plots of data acquired using the direct connection setup, additional to the shunt and interferometer setups, at the mentioned 3 frequencies. At all 3 frequencies, the spreading of the points in complex plane is an indicator of noise, with the most spreading, and hence, the most noise, in the direct connection approach, followed by the shunt and interferometer setups, respectively.

Table III documents the calculated SNR values for the 3 sensing techniques, at 3 frequencies: 4 GHz, 10 GHz, and 14 GHz. Standard shunt setup represents a 2–5x improvement over the direct connection performance, whereas the interferometer improves still by a factor of 2–10x, depending on frequency, the shunt setup SNR. The strong variability of SNR with frequency points to the fact that the transmission line to the SMM probe has a frequency dependent performance therefore plays a considerable role in SNR.

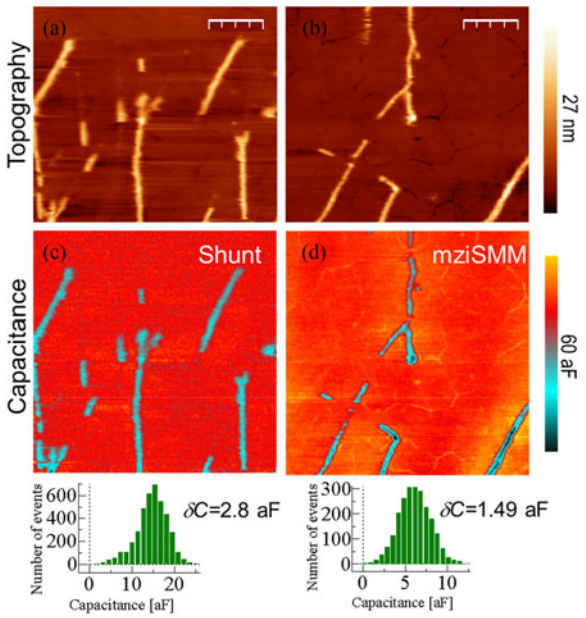

Fig. 6. Imaging mode SNR performance comparison. (a) and (b) Typical AFM topography of several TM viruses on Au substrate. Scale bar in both scans is 0.6 μm. (c) Calibrated capacitance signal obtained using shunt setup (noise distribution is shown below). (d) Calibrated capacitance signal detected using the optimal interferometer setup (noise distribution is shown below). Imaging frequency $f = 19.29$ GHz, $\mathrm{IFBW} = 500$ Hz.

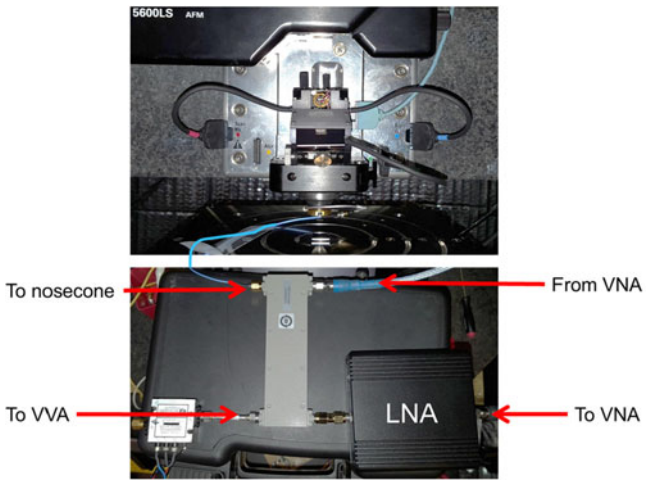

Fig. 7. Picture of the interferometer-SMM setup, including SMM nosecone and scanner (upper panel), and hybrid coupler in the lower panel with the input connection from VNA port 1 (right), the output connection to the LNA (bottom right), the branch feeding the nosecone (left) and the balancing branch with the VVA (bottom left).

VI. APPLICATION: IMAGING SMALL BIO-SAMPLES

Having empirically confirmed the expected superior SNR performance of the interferometer approach, we employed it for testing a sample that previously pushed the limits of shunt setup's sensitivity: Tobacco mosaic virus (TMV), with <300 nm length and <18 nm height, deposited on a gold substrate. Note that the viruses tend to form linearly assembled lines of viruses

with length of up to a few micrometres. The 2 scans on a similar region shown in Fig. 6, both acquired at 19.29 GHz with shunt and interferometer setups respectively, provide information about the topography and the relative capacitance of the viruses, related to their intrinsic dielectric properties. Calibrated capacitance data has been obtained using the mentioned calibration workflow [9] for both techniques. Both scans were performed successively with the same SMM probe, and under the same conditions, such that we can assume that the sensing probe has not been altered. The improved performance of the interferometer setup, which has provided better contrast of the viruses' shapes over the Si substrate, minimising the noise, is as expected, and can be seen in Fig. 6(c) and (d). The noise distribution extracted from a flat part of the image yields a scan speed dependent noise figure of $\delta \mathrm{C}_{\mathrm{shunt}} = 0.12\ \mathrm{aF}/\sqrt{\mathrm{Hz}}$ and $\delta \mathrm{C}_{\mathrm{mziSMM}} = 0.067\ \mathrm{aF}/\sqrt{\mathrm{Hz}}$ corresponding to a value of $\delta \mathrm{C}_{\mathrm{shunt,100\,Hz}} = 1.25$ aF and $\delta \mathrm{C}_{\mathrm{mziSMM,100\,Hz}} = 0.67$ aF at still reasonable scan speed of 0.4 lines/s (256 × 256 pixels).

VII. Conclusion

SMM can characterize electrical properties of nanoscale materials over wide frequency range 1–20 GHz. High SNR is required to resolve nanoscale objects with ever-shrinking dimensions, below 20 nm, which present extreme impedances or capacitances <1 aF. The drawbacks of the current shunt setup, whose sensitivity spectrum is not continuous, with peaks occurring at discrete frequencies, can be overcome using the interferometer approach, which allows for more versatility in frequency tuning, along with 2–8x improvement of the SNR depending on the chosen frequency.

The theoretically predicted SNR improvement is demonstrated using a test Si/SiO_2 sample, in both imaging and spectroscopy modes. SMM images of TMV deposited on gold have been acquired using both shunt and interferometer techniques. The capacitance image acquired using the interferometer detector has a factor of two better SNR, resolving the virus shape over the Si substrate much clearer.

A detailed SNR comparison of different interferometer setups has been performed, in order to identify the noise sources and with the aim of choosing the optimal configuration, both in terms of signal stability and noise levels. We observed that the best performance is produced using an interferometer system containing hybrid coupler, VVS, and LNA. In this configuration the SNR is limited only by the noise figure of the LNA and the power and quality of the VNA source signal. However, higher source power leads to IMD and generates noise in the LNA. For our VNA an input power of −6 dBm led to the best SMM SNR and we expect that more advanced VNAs will improve the noise figure considerably. Additionally, the need of expanding over biological samples has revealed problems related to dielectric relaxation of water. Consequently, the microwave detection tool needs to be tuneable to work in lossy environments with high water content.

VIII. Materials and Methods

The study has been performed using a commercially available 5600LS AFM interfaced with an E8362B Performance Network Analyser (PNA), both from Keysight Technologies (Santa Clara, CA, US). Conductive solid Pt AFM/SMM probes from Rocky Mountains Nanotechnologies (Salt Lake City, UT, US) were employed for all measurements. Tip radii of the used probes were 40–100 nm with spring constants of 18 N/m and 0.3 N/m for virus measurements.

Upon engaging the probe in contact with the sample, a frequency sweep of VNA signal is performed and the desired scanning frequency is chosen. Electrical measurements are done simultaneously with mechanical ones, by scanning the sample surface line by line and acquiring AFM signals, along with VNA signals, typically in 256 or 512 points, each line.

The interferometer was built using a 90-degree hybrid coupler (model 87310B: 1–18 GHz – Keysight Technologies, Santa Clara, CA, US), passive RF component, along with a VVA (voltage controlled, linearized absorptive microwave attenuator model D1958, 60 dB attenuation range, 8–18 GHz – General Microwave, Syosset, NY, US), and a broadband LNA (model N4985A-S30: 100 kHz–30 GHz, 30 dB gain – Keysight Technologies, Santa Clara, CA, US), both active components.

Dialyzed TMV solutions in water (40 μL, concentration: 0.05 mg/mL, strain *vulgare*) have been prepared according to Method B in [29]. TMV solution was incubated for 10 min on template stripped ultraflat gold surfaces [30] and carefully blown dry with nitrogen.

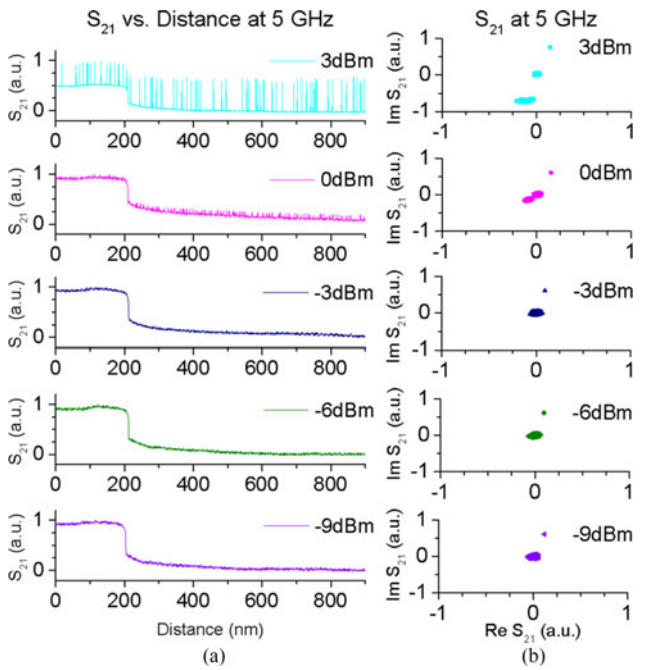

Fig. 8. SNR performance vs. input power comparison. (a) Normalized and corrected S_{21} vs distance curves, performed on bare Si, using hybrid coupler-VVA-LNA setup, at power levels: 3 dBm, 0 dBm, −3 dBm, −6 dBm, −9 dBm. It can be noticed that at 3 dBm and 0 dBm input power, there is a high noise level in the system. Calculated SNR values demonstrate that the least amount of noise in the system occurs at −6 dBm. (b) Complex plane S_{21} scatter plot, for the 5 corresponding power levels.

Appendix

In Fig. 8, a study on the effect of input power level over the observed SNR of the best performing interferometer setup is

presented. The magnitude and complex data of S_{21} normalized vs. tip-sample distance is compared for 5 power levels, from 3 dBm to -9 dBm. Both visualization methods suggest that at positive power levels, there is a high level of noise injected in the system, which decreases with decreasing input power.

Additionally, at the lower end of the tested power levels, the signal level drops, suggesting that the best performance is achieved at -6 dBm. This is supported by the calculated values of SNR for each tested power level, shown in Table II.

ACKNOWLEDGMENT

The authors would like to thank Dr. A. Calò and Prof. A. M. Bittner (nanoGUNE, Spain) for their support on the TMV measurements and the group of Prof. C. Wege (Institute for Biomaterials and Biomolecular Systems, University of Stuttgart) for providing the TMV solutions. The authors also would like to thank Dr. E. Brinciotti, G. Badino, and I. Alic from Keysight Technologies, Austria for the fruitful technical discussions and Prof. P. Hinterdorfer for the AFM related advice.

REFERENCES

[1] C. P. Vlahacos, R. C. Black, S. M. Anlage, A. Amar, and F. C. Wellstood, "Near-field scanning microwave microscope with 100 μm resolution," *Appl. Phys. Lett.*, vol. 69, no. 21, pp. 3272–3274, 1996.

[2] S. M. Anlage, V. V. Talanov, and A. R. Schwartz, "Principles of near-field microwave microscopy," *Scanning Probe Microsc.*, vol. 2, pp. 215–253, 2007.

[3] A. P. Gregory *et al.*, "Recent progress with a near-field scanning microwave microscope," p. 217257, 2011.

[4] J. C. Weber *et al.*, "A near-field scanning microwave microscope for characterization of inhomogeneous photovoltaics," *Rev. Sci. Instrum.*, vol. 83, no. 8, Aug. 2012, Art. no. 83702.

[5] J. Kim, M. S. Kim, K. Lee, J. Lee, D. Cha, and B. Friedman, "Development of a near-field scanning microwave microscope using a tunable resonance cavity for high resolution," *Meas. Sci. Technol.*, vol. 7, 2003, Art. no. 14.

[6] M. Tabib-Azar, D. Akinwande, G. Ponchak, and S. R. LeClair, "Novel physical sensors using evanescent microwave probes," *Rev. Sci. Instrum.*, vol. 70, no. 8, 1999, Art. no. 3381.

[7] C. Gao, T. Wei, F. Duewer, Y. Lu, and X.-D. Xiang, "High spatial resolution quantitative microwave impedance microscopy by a scanning tip microwave near-field microscope," *Appl. Phys. Lett.*, vol. 71, no. 13, 1997, Art. no. 1872.

[8] H. P. Huber *et al.*, "Calibrated nanoscale capacitance measurements using a scanning microwave microscope," *Rev. Sci. Instrum.*, vol. 81, no. 11, Nov. 2010, Art. no. 113701.

[9] G. Gramse, M. Kasper, L. Fumagalli, G. Gomila, P. Hinterdorfer, and F. Kienberger, "Calibrated complex impedance and permittivity measurements with scanning microwave microscopy," *Nanotechnology*, vol. 25, no. 14, 2014, Art. no. 145703.

[10] H. Happy, G. D. Kamel Haddadi, D. Théron, and T. Lasri, "Measurement techniques for RF nanoelectronic devices," *IEEE Microw. Mag.*, vol. 15, no. 1, pp. 30–39, Jan.-Feb. 2014.

[11] S. Gu, T. Lin, and T. Lasri, "Dielectric properties characterization of saline solutions by near-field microwave microscopy," *Meas. Sci. Technol.*, vol. 28, no. 1, 2017, Art. no. 14014.

[12] H. Bakli, K. Haddadi, and T. Lasri, "Modeling and calibration in near-field microwave microscopy for dielectric constant and loss tangent measurement," *IEEE Sens. J.*, vol. 16, no. 12, pp. 4667–4668, Jun. 2016.

[13] H. Tanbakuchi, F. Kienberger, M. Richter, M. Dieudonne, M. Kasper, and G. Gramse, "Semiconductor material and device characterization via scanning microwave microscopy," in *Proc. Int. Symp. IEEE Compd. Semicond. Integr. Circuit*, 2013.

[14] H. Tanbakuchi, M. Richter, F. Kienberger, and H. Huber, "Nano scale materials and device characterization via scanning microwave microscope," in *Proc. Int. Conf. Microw. Commun. Antennas Electron. Syst.*, 2009.

[15] K. Haddadi, S. Gu, and T. Lasri, "Sensing of liquid droplets with a scanning near-field microwave microscope," *Sens. Actuators A, Phys.*, vol. 230, pp. 170–174, 2015.

[16] T. Dargent *et al.*, "An interferometric scanning microwave microscope and calibration method for sub-fF microwave measurements," *Rev. Sci. Instrum.*, vol. 84, no. 12, 2013, Art. no. 123705.

[17] G. Vlachogiannakis, H. T. Shivamurthy, M. A. Del Pino, and M. Spirito, "An I/Q-mixer-steering interferometric technique for high-sensitivity measurement of extreme impedances," in *Proc. 2015 Int. Symp. IEEE MTT-S Microw.*, 2015.

[18] K. Haddadi, C. Brillard, G. Dambrine, and D. Theron, "Sensitivity and accuracy analysis in scanning microwave microscopy," in *Proc. Int. Symp. IEEE MTT-S Microw.*, 2016.

[19] M. Randus and K. Hoffmann, "A simple method for extreme impedances measurement–Experimental testing," in *Proc. 2008 72nd Int. Symp. ARFTG Microw. Meas.*, 2008, vol. 2, pp. 40–44.

[20] M. Randus and K. Hoffmann, "Microwave impedance measurement for nanoelectronics," *Radioengineering*, vol. 20, no. 1, pp. 276–283, 2011.

[21] S. Tamaru, K. Yakushiji, A. Fukushima, S. Yuasa, and H. Kubota, "Ultrahigh sensitivity ferromagnetic resonance measurement based on microwave interferometer," *IEEE Magn. Lett.*, vol. 5, 2014, Art. no. 3700304.

[22] A. Wirthmann *et al.*, "Direct phase probing and mapping via spintronic michelson interferometry," *Phys. Rev. Lett.*, vol. 105, no. 1, pp. 1–4, 2010.

[23] G. Gramse *et al.*, "Quantitative sub-surface and non-contact imaging using scanning microwave microscopy," *Nanotechnology*, vol. 26, no. 13, 2015, Art. no. 135701.

[24] J. Hoffmann, G. Gramse, J. Niegemann, M. Zeier, and F. Kienberger, "Measuring low loss dielectric substrates with scanning probe microscopes," *Appl. Phys. Lett.*, vol. 105, no. 1, pp. 1–5, 2014.

[25] S.-S. Tuca *et al.*, "Calibrated complex impedance of CHO cells and E. Coli bacteria at GHz frequencies using scanning microwave microscopy," *Nanotechnology*, vol. 27, no. 13, 2016, Art. no. 135702.

[26] E. Brinciotti *et al.*, "Probing resistivity and doping concentration of semiconductors at the nanoscale using scanning microwave microscopy," *Nanoscale*, vol. 7, no. 35, pp. 14715–14722, 2015.

[27] Agilent Technologies, "Agilent network analyzer basics," Agilent Technologies, Santa Clara, CA, USA, 2004, pp. 1–94.

[28] Analyzers Agilent PNA Microwave Network, "Agilent E8362B data sheet." [Online]. Available: http://cp.literature.agilent.com/litweb/pdf/5988-7988EN.pdf

[29] A. Kadri *et al.*, "Engineered Tobacco mosaic virus mutants with distinct physical characteristics in planta and enhanced metallization properties," *Virus Res.*, vol. 157, no. 1, pp. 35–46, 2011.

[30] M. Hegner, P. Wagner, and G. Semenza, "Ultralarge atomically flat template-stripped Au surfaces for scanning probe microscopy," *Surf. Sci.*, vol. 291, nos. 1–2, pp. 39–46, 1993.

Authors' photographs and biographies not available at the time of publication.